2018-06-18

Analysis of electrospinning bending region physics in determining fiber diameter: focus on mass transfer and effect of relative humidity for non-aqueous hydrophilic solutions

Analysis of Electrospinning Bending Region Physics in Determining Fiber Diameter: focus on mass transfer and effect of relative humidity for non-aqueous hydrophilic solutions

Yunshen Cai and Michael Gevelber
Department of Mechanical Engineering
Boston University, Boston

Abstract:

This paper analyzes the bending region of non-aqueous hydrophilic PVP/alcohol solutions, using a combined experimental and modeling approach. A major focus of this work is modeling the complex mass transport including solvent evaporation and water absorption, which is verified by evaporation experiments. The developed model captures the coupled mass and force balances in the bending region and predicts the final fiber diameter to within 8% of experimental measurements for three different PVP/alcohol solutions with significantly different properties. The model analysis reveals the effect that RH has on alcohol evaporation rate, which affects both net stretching force and jet length in determining the final fiber diameter.

1. Introduction

This paper studies the role of the electrospinning bending region in determining fiber diameter for non-aqueous hydrophilic PVP/alcohol solutions. The electrospinning process first typically forms a straight jet from a charged polymer/solvent solution, followed by a circular moving jet in the shape of a cone, called the bending region. The process physics in the bending region is challenging to study since the jet diameter cannot be measured directly due to its rapid motion and small size (~micron and smaller), and due to the complex coupling between the multiple forces, mass transport, and changing jet geometry. For hydrophilic polymer solvent systems, there is an additional complexity since the solvent absorbs water, and experimentally, it is well known that ambient relative humidity (RH) significantly affects the process. To develop a more explicit understanding of the process physics, a bending region model is developed which predicts the jet behavior and

fiber diameter for three solutions (PVP/methanol, PVP/ethanol and PVP/1-butanol) for a variety of process conditions, including RH. The model is validated by experiments conducted for those three solutions, which have significantly different properties, over a broad range of operating conditions. Analysis of the model results provides insight into how the net evaporation rate affects the bending region jet length and net stretching force, both of which ultimately determines the fiber diameter, as well as the impact of RH.

There have been a number of electrospinning process models developed that relate forces to fiber diameters. Hohman, et al. [1, 2] developed a slender-body model for both straight jet and bending regions that captures jet stretching, charge transport, and the electric field. Their model includes three competing factors: extensional viscous stress, surface tension, and electrostatics. In the bending region, they considered the change of force and electric field due to the jet motion, but they do not consider the mass transfer/ evaporation, nor the impact of RH. For the straight jet region, Feng [3] simplified the slender body model for Newtonian jets using an approximation for the electric field equation, and predicted jet behavior. His differential format of the steady-state momentum equation provides the basis to analyze force balance in the bending region in this research.

Fridrikh, et al. [4] analyzed Hohman's dynamic equations for the whipping jet to obtain an asymptotic solution that relates the final fiber diameter to operating conditions, based on a balance between normal stresses due to surface tension and surface charge repulsion yielding: $d_{fiber} \sim \left(\frac{I}{Q}\right)^{-\frac{2}{3}}$. The analysis does not include a viscous term, since it is argued that in the terminal state of electrospinning process, the viscous force is relatively small and does not determine fiber diameter. They also did not explicitly consider mass transfer effects due to evaporation rate, although it is expected to determine jet length.

It is well known experimentally that RH can have a significant impact on the electrospinning process and resulting fiber diameters. For some hydrophilic polymers in hydrophilic solvent systems, the electrospun fiber diameters decrease as RH increases [5-7]. De Vrieze, et al. [5] experimentally found that fiber diameters of PVP (hydrophilic) in alcohol (hydrophilic) solutions decrease with increasing RH. They state that the fiber diameter decreases at higher humidity since the absorption of water increases the time of flight of the polymer solution jet. However, they do not analyze the amount of water absorbed under different RH conditions, nor the effect of water absorption on jet stretching.

Cai et al. [6] experimentally found that fiber diameters of PVP/alcohol solutions decrease with increasing RH. They present a fiber diameter correlation for PVP/alcohol solutions based on measurable process parameters (upper jet diameter) and RH. However, they did not determine how RH affects the process physics that determines final fiber diameters.

Wang [7] electrospun polystyrene (PS) in THF and DMF solvents to investigate the influence of solution and process parameters on the jet diameter ($d_{S,jet}^{final}$), measured at the end of straight jet region, and fiber diameter (d_{fiber}). They found that $d_{fiber} \sim m \cdot d_{S,jet}^{0.45}$, where $m \sim \eta_0^{0.38} K^{0.12}$, in terms of η_0 the shear viscosity, K the conductivity, and solution viscosity. However, they did not explicitly analyze how solution and process parameters affect the force balance, nor the effect of evaporation and RH.

To examine the effect of RH, a model of mass transport in the bending region is needed. The major challenge for PVP/alcohol solutions is to model mass transfer which includes absorption/evaporation of water and alcohol, radial diffusion of both species in the jet, and axial advection.

Yarin, et al. [8] proposed a model for solvent evaporation and solidification in an electrospinning jet by relating solvent evaporation coefficient to Sherwood number. They considered the change of momentum and viscosity due to evaporation. However, they did not explicitly analyze the effect of evaporation and RH on charge density and strain rate relative to electric and viscous forces, nor explicitly analyze a second species (e.g. water) absorbed by the solvent. Forward et al. [9] provides a mass transport model for the solidification of a co-axial jet, where the core solvent (water) diffuses through the shell solvent and both solvents evaporate at the outermost surface. Although they did not analyze water absorption by a solvent, their work on the water diffusion and solvent evaporation provides a basis for our water absorption and solvent evaporation model development.

2. Experimental approach

Electrospinning experiments are conducted with 12wt% PVP/methanol, PVP/ethanol and PVP/1-butanol solutions in a system with controlled RH. The electrospinning system includes the capability of monitoring multiple process states in real-time and setting actuator set points for the syringe pump (Harvard Apparatus, PHD 2000), high voltage

power supply (HV POWER SUPPLY, XRM30P) [10]. A salt bath (magnesium chloride) system and a water vapor system [11] are used to adjust the experimental RH level. Magnesium chloride powders absorb water vapor from the ambient air to decrease the ambient RH. Water vapor generated by a water heating system is used to increase the ambient RH.

Two CCD cameras are used to measure the jet diameters in straight jet region. Jet current is measured by a current sensor, which is placed between the fiber collector and NI USB-6008 data acquisition (DAQ) card [10,11,12]. The ambient RH and temperature are monitored by HTM 2500 in real-time. Achieved electrospun fiber diameters are imaged using a Zeiss SUPRA 40VP FESEM (Field Emission Scanning Electron Microscope).

2.1 Materials

PVP with 1,300k molecular weight were dissolved in different alcohol (methanol, ethanol and 1-butanol) solvents to make 12wt% PVP/alcohol solutions. PVP powders and all alcohol solvents were purchased from the Aldrich Chemical Co. All solutions were stored in a refrigerator at 5 ℃. Before experiments, solutions were put in the ambient environment for several hours to bring the solutions to room temperature (21 – 24 ℃). All electrospinning experiments are also conducted at ambient room temperature.

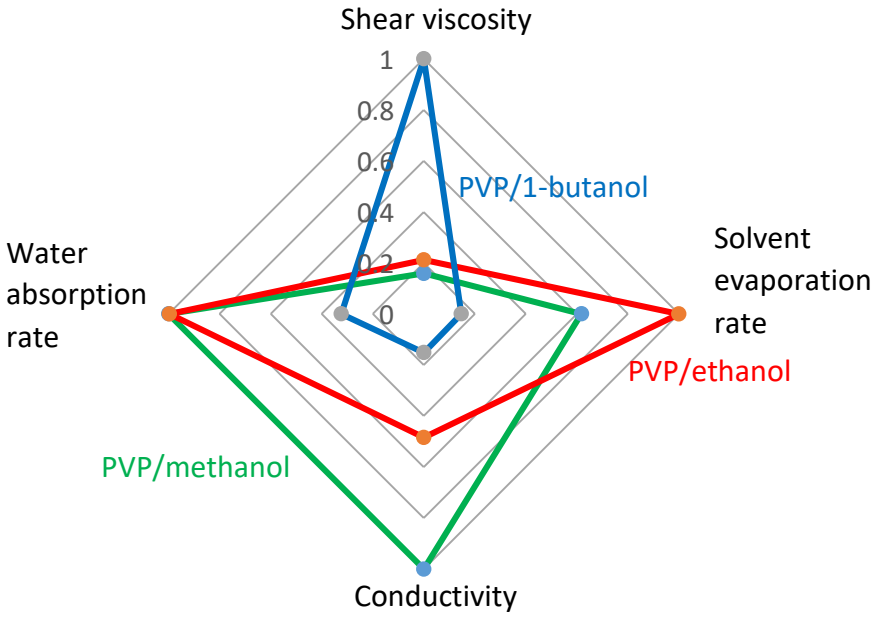

Fig. 1 Normalized characteristic parameters of PVP/alcohol solutions, in terms of shear viscosity, conductivity, solvent evaporation rate and water absorption rate.

Parameters of the PVP/alcohol solutions are shown in fig. 1, in terms of shear viscosity, conductivity, solvent evaporation rate and water absorption rate, normalized by the maximum value. The shear viscosity measurements were performed in a cone-plate viscometer (TA Instruments AR2000). The conductivities are measured by a conductivity sensor (TDTestr 40). The alcohol evaporation rates are published in a handbook of organic solvent properties [13], which are also verified by alcohol evaporation experiments under 10% RH (described in appendix. B). The water absorption rates are estimated based on water diffusivities in alcohol (see section 3).

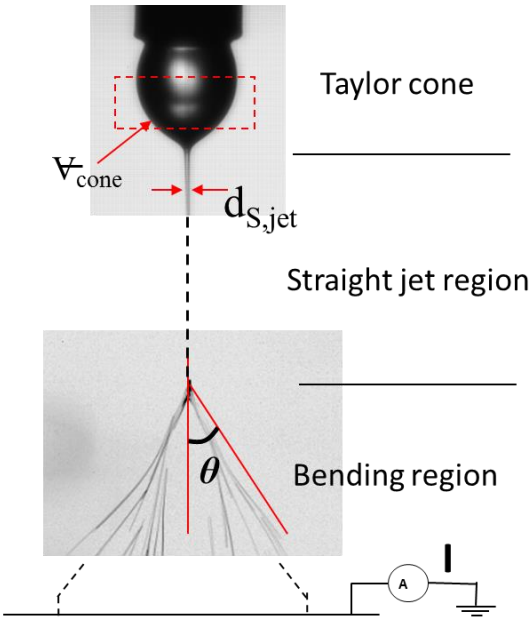

Fig. 2 Measurable process parameters

2.2 Experimental results and implications

Fig. 2 shows the measurable parameters of the system. The interaction of the electrostatic forces and the surface tension of the liquid create a 'Taylor' cone at the end of the needle, which can be measured with a characterized Volume ($\forall$) [10]. When the electrical force is larger than the surface tension, a jet emerges from the Taylor cone and is accelerated due to Coulomb forces [10]. The straight jet is characterized by the jet diameter at specific length ($d_{S,jet}^{3mm}$ at 3 mm point from the needle as well as $d_{S,jet}^{final}$ at the end of straight jet region).

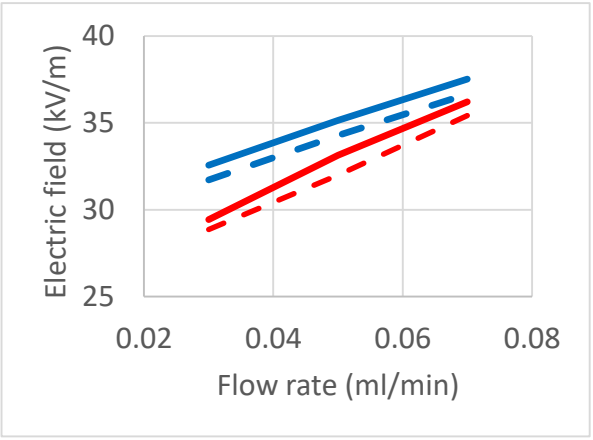

Fig. 3 Electric field operating bounds: upper (full line) and lower (dash line) for PVP/ethanol solutions under 25% RH (red) and 50% RH (blue).

At a critical length, perturbations are not cancelled and the bending region starts. This can be characterized by a bending angle (θ) [10]. To measure the fiber current (I), a current sensor is placed between the collector and NI USB-6008 data acquisition (DAQ) card.

Applied voltage, flow rate and RH are major controllable parameters in the electrospinning process. To identify the allowable operating bounds for a given RH level and flow rate, voltage was varied from low to high in order to determine the upper and lower electric field bounds, between which electrospinning will occur with small variation [10]. Below the lower voltage bound, there is a large variation in Taylor cone volume and falling droplets. Above the upper voltage bound, the Taylor cone is not observed, and the jet originates directly within the needle and sometimes it moves around the edge of the needle tip. This procedure is repeated for different flow rates to obtain the allowable operating bounds diagram under a constant RH. The operating bounds of solutions vary with RH (fig.3), since RH affects the jet current and the electric force.

We also are interested in determining how to relate operating conditions and measurable process parameters to predict the final fiber diameter. As described in our early paper [14] for PEO/water solutions, the diameter of the upper straight jet diameter near the Taylor cone ($d_{S,jet}^{3mm}$) can be used as part of a correlation to the fiber diameter (d_{fiber}). Since little evaporation occurs in the straight jet region, the measured jet diameter is believed to characterize the viscous-electric force balance. The other factor used in the correlation is proportional to solvent evaporation rate. A linear correlation is achieved (fig.4), if $(1 - RH)^2$ is used. This correlation suggests that there is a generalizable process physics relationship, and also raises a question of how does RH affect the final fiber diameter?

Since alcohol is hydrophilic, the second order RH dependence suggests that water absorption strongly affects the process physics.

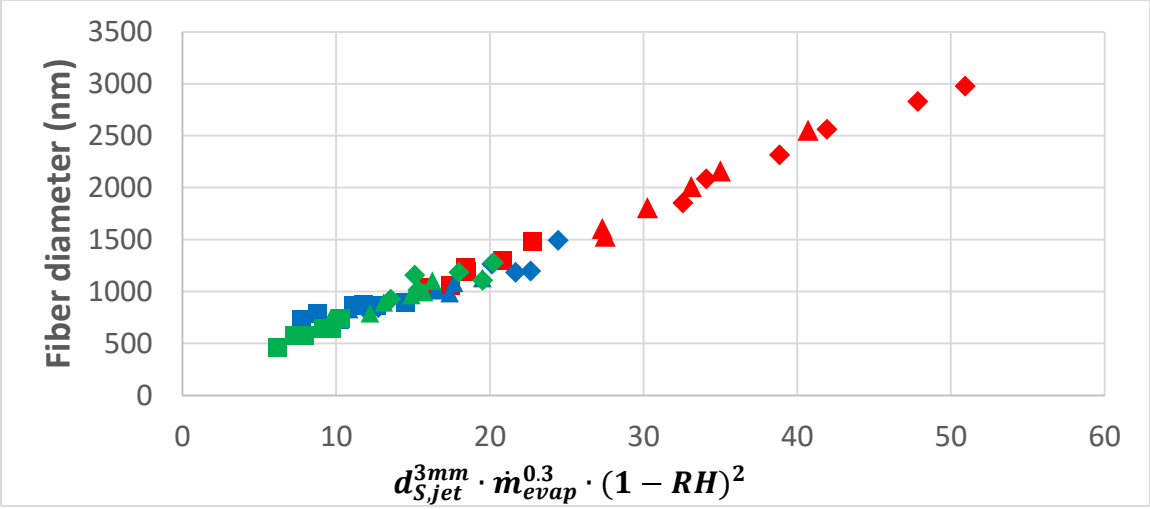

Fig. 4 Correlation of fiber diameters to measurable parameters for PVP/alcohol solutions: (a) correlation based on straight jet diameters; (b) correlation based on straight jet diameters and solvent evaporation rate; (c) correlation based on straight jet diameter, solvent evaporation rate as well as RH. Blue : PVP/methanol; Green : PVP/ethanol; Red: PVP/1-butanol; ◆: 25% RH; ▲: 35% RH; ■: 50% RH

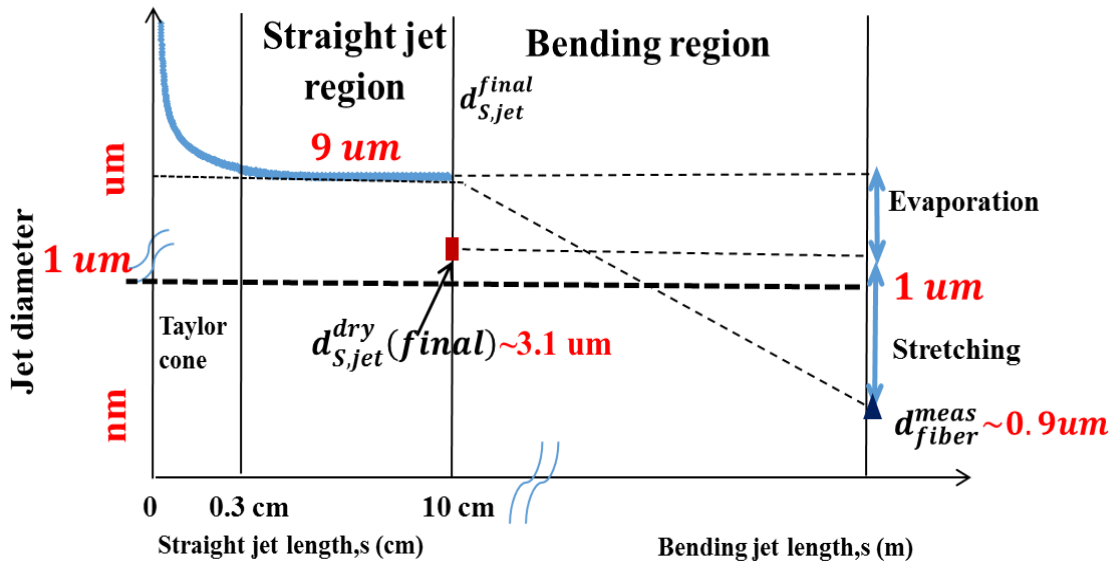

Fig. 5. Illusion of jet stretching in straight jet region and bending region. Final dry diameter based on the jet diameter at the end of straight jet region reveals that stretching is significant to determine final fiber diameter in the bending region. (based on PVP/ethanol results)

The role of the bending region relative to straight jet region in terms of stretching and solvent evaporation is illustrated in Fig. 5, based on PVP/ethanol experimental data (see appendix A of [12]). The $d_{S,jet}^{dry}(final)$ is the jet diameter if the solvent were removed at the end of straight jet region, and represents the fiber diameter if there was no stretching in

the bending region. $d_{S,jet}^{dry}(final)$. Table.1 gives the values for the 3 solvent (4 - 10 μm), which are much larger than the final fiber diameters (1 - 3 μm). for PVP/methanol, PVP/ethanol and PVP/1-butanol solutions. Thus, the stretching in the straight jet region cannot explain the final fiber diameter, and jet stretching is significant in the bending region. The ratio of the jet cross surface area change with solvent removed in the straight jet region ($R_{straight} = \frac{A_{S,jet}^{dry}(final)}{A_{S,jet}^{dry}(3mm)}$) and in the bending region ($R_{bending} = \frac{A_{fiber}^{meas}}{A_{S,jet}^{dry}(final)}$) show that ~51% of jet stretching occurs in the bending region for PVP/alcohol solutions.

In contrast, the degree of solvent evaporation in the straight jet region can be evaluated by the ratio of solvent evaporation rate in the straight jet region ($\dot{m}_{S,evaporation}^{solvent}$) over the jet solvent flow rate ($Q \cdot (1-c)$), as $\%\text{Evap}_{SJR} = \frac{\dot{m}_{S,evaporation}^{solvent}}{Q \cdot (1-c) \cdot \rho}$, where Q is the infuse rate of solution; c is the initial polymer concentration; ρ is solution density; $\dot{m}_{S,evaporation}^{solvent}$ is solvent evaporation rate in straight jet region, which is determined by the solvent evaporation rate per area [13] and the jet surface area. The jet surface area is determined by the measured straight jet shape.

Based on the solvent evaporation rate, the calculated degree of solvent evaporation in the straight jet region for different PVP/alcohol solutions, are all less than 1%. Thus, the bending region is significant in determining the fiber diameter, in terms of essentially all the evaporation and half of the jet stretching.

Table. 1 Degree of stretching impact on fiber deformation in bending region

Materials	PVP/methanol	PVP/ethanol	PVP/butanol
$d_{S,jet}^{\text{dry}}(3mm)$ (μm)	17	23.2	30.6
$d_{S,jet}^{dry}(final)$ (μm)	3.78	4.96	10.1
d_{fiber}^{meas} (μm)	1.22	1.89	2.59
$R_{straight} = \frac{A_{S,jet}^{dry}(final)}{A_{S,jet}^{dry}(3mm)}$	4.9%	4.6%	11%
$R_{bending} = \frac{A_{fiber}^{meas}}{A_{S,jet}^{dry}(final)}$	10%	14%	6.6%

3. Bending region model

A model is developed, capturing the coupled mass and force balances, to get insight into the process physics. Since alcohol is a hydrophilic solvent, it absorbs water from the surrounding moisture air, and both the alcohol solvent and the absorbed water must evaporate to achieve the final dry fibers.

3.1 Mass transfer: water absorption and solvent evaporation

Due to the hydrophilic nature of alcohol, the mass transfer for a stationary alcohol liquid includes the water vapor flux (J_{air}^{water}), alcohol vapor flux ($J_{air}^{solvent}$) in the air, and the water diffusion ($J_{solution}^{water}$), alcohol diffusion ($J_{solution}^{solvent}$) in the solution.

The water and alcohol fluxes in air (J_{air}^{i}) and the fluxes in solution ($J_{solution}^{i}$) are described by an empirical equation (1) and Fick's first law equation (2) respectively;

$$J_{air}^{i} = h_i \cdot A \cdot (c_{surf}^{i}(\mathrm{v}) - c_{air}^{i}(\mathrm{v})) \cdot Mw_i \quad (1)$$

$$J_{solution}^{i} = D_i \cdot A \cdot \nabla c^{i}\ (l) \cdot Mw_i \quad (2)$$

where h_i is the mass transfer coefficient of water (solvent), which is related to Sherwood number [6]; A is the surface area; Mw_i is molecular weight of water or solvent; D_i is the water diffusivity in alcohol; $c_{surf}^{i}(\mathrm{v})$ is the mole concentration of water (solvent) vapor in the vapor phase; $c_{air}^{i}(\mathrm{v})$ is the mole concentration of water (solvent) vapor in the ambient air; $c^{i}\ (l)$ is the water (solvent) mole concentration in liquid phase; $\nabla c^{i}\ (l)$ is the water mole concentration gradient in the liquid.

Equation (1) reveals that mass transfer in the air is determined by the water or solvent vapor mole concentration difference between ambient air (c_{air}^{i}) and solution surface in the vapor phase ($c_{surf}^{i}(\mathrm{v})$). Assuming that the water vapor (c_{air}^{water}) and alcohol vapor ($c_{air}^{solvent}$) mole concentrations in ambient air are constant (since the amount of absorbed water and evaporated alcohol is relatively small), the only unknown parameters for determining water and solvent fluxes in air (J_{air}^{i}) are the water and solvent vapor mole concentrations on the surface. Equation (2) indicates that the diffusion in the solution is driven by the water and solvent mole concentration gradients ($\nabla c^{i}\ (l)$) in the liquid, which are the only unknown parameters to determine the water and solvent fluxes in solution ($J_{solution}^{i}$).

Thus, the only unknown parameters for the mass transfer are surface conditions, including water and solvent mole concentrations and their gradients. The relation between $c^i_{surface}(\mathrm{v})$ and $c^i_{surface}(l)$ is given by Raoult's law as:

$$c^i_{surface}(\mathrm{v}) \cdot P = c^i_{surface}(l) \cdot \gamma_i \cdot P^i_{saturated} \cdot \frac{Mw_{solution} \cdot \rho_{air}}{Mw_{air} \cdot \rho_{solution}} \qquad (3)$$

where P is the air pressure; $P^i_{saturated}$ is the saturated pressure of water (solvent) vapor in air; γ_i is the correlation for interactions in liquid phase between different molecules, called activity coefficient, which is used to modify the fractions or concentrations of components in a mixture. In a non-ideal mixture, the microscopic interactions between each pair of chemical species are not same (e.g. the enthalpy change of solution in mixing is not zero), and thus properties of the mixtures cannot be expressed directly in terms of simple concentrations or partial pressures. There are several methods to determine the activity coefficient of solvents systems. In this paper, a UNIVERSAL Functional Activity Coefficient (UNIFAC) model [15] is used to calculate the activity coefficient of each solvent where $Mw_{solution}$ is the solution molecular weight, Mw_{air} is the air molecular weight, $\rho_{solution}$ is the solution density and ρ_{air} is the air density.

To determine the surface state, the dynamic of water (or solvent) mole concentration on surface is calculated from the difference in air and solution flows by:

$$\frac{dc^i_{surface}}{dt} = \frac{J^i_{air} - J^i_{solution}}{Mw_i \cdot A \cdot dh} \qquad (4)$$

where h is the solution depth.

To determine which flux limits the water absorption for a stationary liquid, the relation between resistances of the air (R^{water}_{air}, equation (5)) and liquid ($R^{water}_{solutions}$, equation (6)) mass transfer are evaluated, in order to calculate the mass transfer Biot number, ($Bi_m = R^{water}_{solution}/R^{water}_{air}$). The calculated Bi_m for a stationary liquid with 0.5 μ m is 4 (corresponding to the typical fiber diameter 1 μm), for 50 μm its 328 (corresponding to the typical upper jet diameter 100 μm), and for 7 mm its 45,900 (corresponding to the stationary alcohol liquid depth used in evaporation experiments discussed later in this section) depth. Although the Bi_m decreases as liquid depth decreases, $R^{water}_{solution}$ is much

larger than R_{air}^{water} even when the liquid depth is only 0.5 μm, which suggests that the water absorption is limited by the water diffusion in the solution.

$$R_{air}^{water} = \frac{1}{h_w \cdot A \cdot Mw_{water}} \quad (5)$$

$$R_{solutions}^{water} = \frac{h \cdot P_{saturated}^{water} \cdot \gamma_{water} \cdot Mw_{solution} \cdot \rho_{air}}{D_i \cdot A \cdot P \cdot \rho_{solution} \cdot Mw_{water} \cdot Mw_{air}} \quad (6)$$

2-D lumped model for an alcohol jet mass transfer in the bending region

For a polymer/solvent jet, the mass transfer analysis must be extended to consider the jet shape. The water diffusion in the jet is analyzed in cylindrical coordinate with different boundary conditions. The analytical water concentration in a jet without axial advection (no solution flow) is a function of radius (r) and time (t), expressed as: $c^{water} \sim \int_{\infty}^{\xi} \frac{1}{\xi^*} e^{-\frac{\xi^{*2}}{4}} d\xi^*$, where $\xi^* = \frac{r}{\sqrt{D_i t}}$. Analysis of the analytical solution to the water concentration profile as a function of time in a jet with 5 μm radius under 50% RH, reveals that the absorbed water mole concentration in the jet is not uniform. Since the water absorption is limited by water diffusion in the jet ($Bi_m \gg 1$), it is required to determine the water mole concentration profile in the jet to capture the water diffusion. A lumped model to describe the mass transfer in jet using a set of 3 radial lumps ($\Delta R_1 : \Delta R_2 : \Delta R_3$ = 5:4:1 from jet surface to jet central) are used. The modeled water concentration profile is compared to the analytical water concentration profile, and indicates that the 3 radial lumps captures the water diffusion in the jet [12].

To capture the axial advective flux of water and alcohol due to the jet solution flow and the radial diffusive flux of water and alcohol cross the jet, a 2-D lumped model (fig. 6) is used to determine the water and alcohol mole concentration profiles and the mass transfer rates for a n-th set of jet radial lumps with 1mm lump length. The determination for the lump length is given in appendix D of [12].

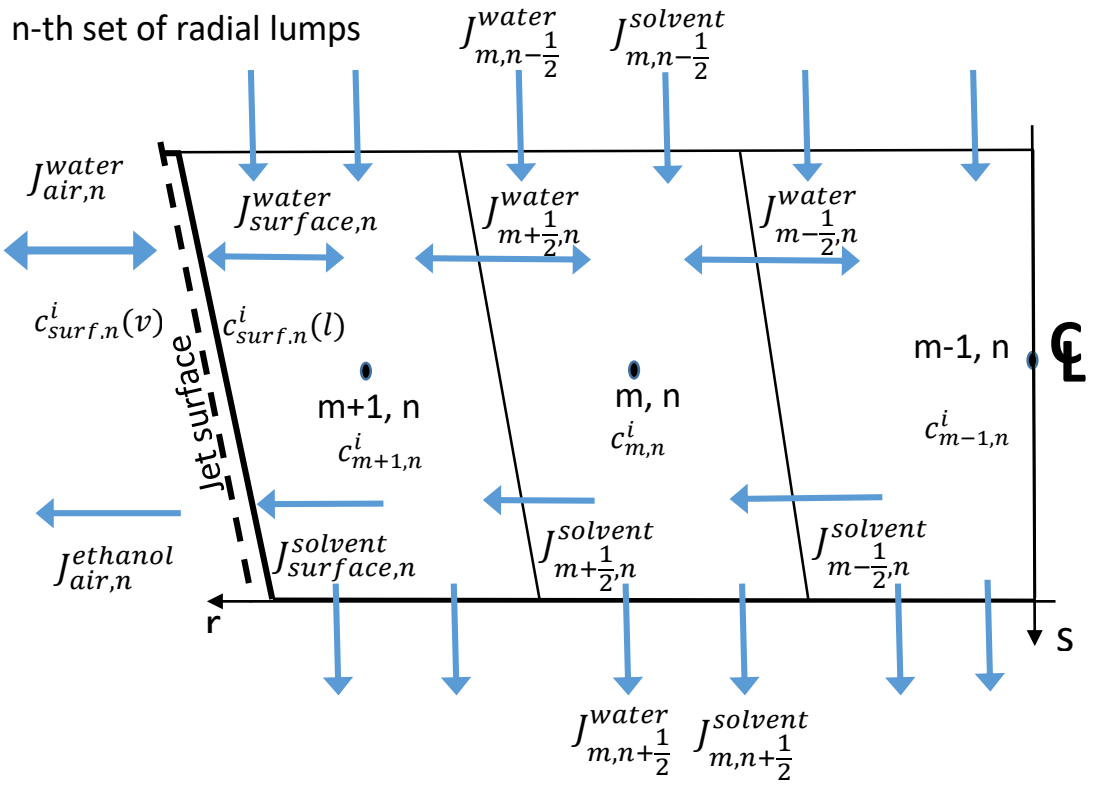

Fig. 6 Sketch illustrating two-dimensional numerical analysis of water absorption and solvent evaporation for n-th set of radial lumps

For a set of 3 radial lumps section, there are eight unknown parameters which are water and solvent mole concentrations on surface ($c^{i}_{surf,n}$) and water and solvent mole concentrations in each of the 3 radial lumps ($c^{i}_{m+1,n}$, $c^{i}_{m,n}$, and $c^{i}_{m-1,n}$). The unknown lump states are determined by iteratively solving the mass balance equations in each lump and on surface until a convergence is achieved (see chapter 7 in [12]). Once the lump states are determined, the mass fluxes in terms of evaporation and absorption of water and alcohol surface, the radial diffusion and axial advection are determined based on the fluxes functions.

The evaporation and absorption of alcohol and water on surface are two significant fluxes we are interested in, since they determine how much water is absorbed, the total axial jet flow rate, and how fast the jet solidifies. Once the water and solvent mole concentrations on the n-th set of 3 radial lumps surface ($c^{i}_{surf,n}$(v)) are calculated, the water absorption rate and alcohol evaporation rate on n-th set of 3 radial lumps surface (equation (1)) can be determined from:

$$\dot{m}_n^{water} = J_{air,n}^{water} = h_w \cdot A_n \cdot \left(c_{surf,n}^{water}(\mathrm{v}) - c_{air}^{water}\right) \cdot Mw_{water}$$
$$= 1.95 v_a^{\frac{1}{6}} \cdot v_{air}^{\frac{1}{3}} \cdot R_n^{\frac{1}{3}} \cdot \left(c_{surf,n}^{water}(\mathrm{v}) - RH \cdot \frac{P_{saturated}^{water}}{R_{air} \cdot T}\right) \cdot D_{water-air}^{\frac{1}{2}} \cdot Mw_{water} \cdot ds \quad (7)$$

$$\dot{m}_n^{solvent} = J_{air,n}^{solvent} = h_s \cdot A_n \cdot \left(c_{surf,n}^{solvent}(\mathrm{v}) - c_{air}^{solvent}\right) \cdot Mw_{solvent}$$
$$= 1.95 v_a^{\frac{1}{6}} \cdot v_{air}^{\frac{1}{3}} \cdot R_n^{\frac{1}{3}} \cdot c_{surf,n}^{solvent}(\mathrm{v}) \cdot D_{solvent-air}^{\frac{1}{2}} \cdot Mw_{solvent} \cdot ds \quad (8)$$

where v_a is the kinematic viscosity of air; ds is the differential jet length; R_{air} is ideal gas constant; T is the temperature; v_{air} is the air cross velocity, 10m/s, which is determined in [6]. Equation (7) reveals that the water will start to evaporate from the jet surface, when the water vapor mole concentration on the n-th set of 3 radial lumps surface is larger than the ambient water vapor mole concentration. By assuming that the solvent vapor mole concentration in air is 0, and both water and solvent vapor concentrations do not change in the air concentrations (since the amount of absorbed water and evaporated alcohol is relatively small), the net evaporation rate for the n-th set of 3 radial lumps is:

$$\dot{m}_{net,n} = -dQ \cdot \rho_{solution} = \dot{m}_n^{solvent} + \dot{m}_n^{water} \quad (9)$$

which is a function of jet flow rate (Q) and jet radius (R).

3.2 Force balance

In the bending region, the differential equation (10) for force balance is built on the work of Hohman [1, 2] and Feng [3]. To numerically solve the force balance differential equation for the bending region, the bending region jet is cascaded into discrete sets of 3 radial lumps with a short length ds. The force balance performed on each node requires the net force acting on the set of 3 radial lumps is equal to the change of momentum that fluxes in and out the set of radial lumps. For the n-th set of 3 radial lump in the bending region, although the water and alcohol mole concentration profiles in the 3 radial lumps are not uniform, the average lump parameters (e.g. polymer concentration, viscosity and jet flow velocity) are assumed to be uniform in the force balance equation.

To determine the change in jet shape, a force balance is developed from a steady state momentum equation for each lump in the bending region. Our previous analysis [6] has identified the dominant force terms in the bending region, including the extensional viscous force (F_{vis}), charge-to-charge force (F_{charge}) and electric field force ($F_{e\text{-}field}$) (fig. 7). The steady state momentum equation in the bending region is expressed:

$$\underset{(1.\ \frac{DM}{Dt})}{\frac{\rho v_s}{\pi R^2}\frac{d}{ds}(Q)} + \rho v_s \frac{d}{ds}(v_s) = \underset{(2.\ F_{vis})}{\frac{3}{R^2}\frac{d}{ds}(R^2\eta^*\frac{d}{ds}v_s)} + \underset{(3.\ F_{charge})}{\left[\frac{\sigma_s}{\bar{\epsilon}}\frac{d}{ds}\sigma_s - \frac{2\sigma_s}{\bar{\epsilon}R}\frac{d}{ds}(R\sigma_s)\right]} + \underset{(4.\ F_{e\text{-}field})}{\frac{2\sigma_s E_\infty}{R}sin\alpha} \quad (10)$$

where $\frac{DM}{Dt}$ is material derivative of momentum; jet flow velocity (v_s) is determined by jet flow rate and jet radius, $v_s = \frac{Q}{\pi R^2}$; Surface charge density (σ_s) is a function of measured jet current, and jet radius, $\sigma_s = \frac{IR}{2Q}$ [7].

In the bending region, equation 10 indicates that the momentum change equals to the sum of the extensional viscous retarding force (term 2) and the electric stretching force in terms of electric field force (term 4) and charge-to-charge force (term 3). The steady state momentum equation is consistent with the work of Hohman [1] and Feng [3] except for addition of 3 factors: a) the helix angle (α) in terms of the electric field force (4. $F_{e-field}$), b) the charge-to-charge force (3. F_{charge}) term is expanded to include the axial charge-to-charge force ($F_{charge}^{axial} = -\frac{2\sigma_s}{\bar{\epsilon}R}\frac{d}{ds}(R\sigma_s)$), which is a significant stretching force in the bending region. (It is noted that the additional axial term in the charge-to-charge force acts opposite to the term given in Feng's equation, and thus, acts to stretch the jet) c) the effect of evaporation on the change of momentum ($\dot{M} = \frac{\rho v_s}{\pi R^2}\frac{d}{ds}(Q) + \rho v_s \frac{d}{ds}(v_s)$). In the straight jet region, since evaporation is negligible ($\frac{d}{ds}Q = 0$), the momentum change on the left hand side can be reduced to $\dot{M} = \rho v_s \frac{d}{ds}(v_s)$, which is consistent with Feng's equation [3]. In the bending region, the momentum change due to the evaporation is also significant.

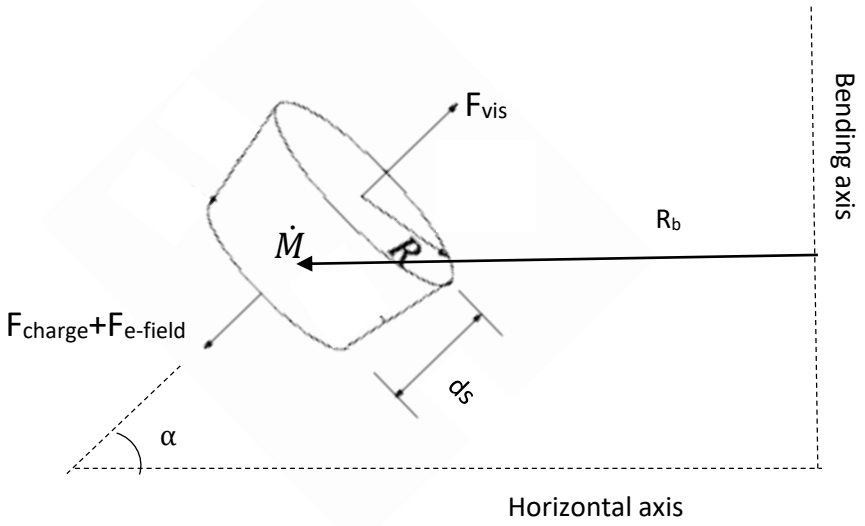

Fig. 7. Force balance for a set of radial lumps in the bending region

The force balance can be rewritten as a function of jet radius (R) and jet flow rate (Q) in order to explicitly indicate how the jet radius varies in terms of change of forces along the jet, by coupling the mass and force balances:

$$\left[\frac{\boldsymbol{2\rho Q}}{\boldsymbol{\pi^2 R^4}}\frac{\boldsymbol{dQ}}{\boldsymbol{ds}} - \frac{2\rho Q^2}{\pi^2 R^5}\frac{dR}{ds}\right] = \left[-\frac{\boldsymbol{6\eta^*}}{\boldsymbol{\pi R^3}}\frac{\boldsymbol{dR}}{\boldsymbol{ds}}\frac{\boldsymbol{dQ}}{\boldsymbol{ds}} + \frac{\boldsymbol{3\eta^*}}{\boldsymbol{\pi R^2}}\frac{\boldsymbol{d^2Q}}{\boldsymbol{ds^2}} + \frac{6\eta^* Q}{\pi R^4}\left(\frac{dR}{ds}\right)^2 - \frac{6\eta^* Q}{\pi R^3}\frac{d^2R}{ds^2}\right] + \left[-\frac{3I^2R}{4\epsilon Q^2}\frac{dR}{ds} + \frac{\boldsymbol{I^2R^2}}{\boldsymbol{4\epsilon Q^3}}\frac{\boldsymbol{dQ}}{\boldsymbol{ds}}\right]$$

(1. $\dot{M}$) (2. F_{vis}) (3. F_{charge})

$$+\left[\frac{E_\infty I \sin\alpha}{Q}\right] \quad (11)$$

(4. $F_{e\text{-}field}$)

where I is measured jet current; $\bar{\epsilon}$ is permittivity of air; E_∞ is the ambient electric field; α is the helix angle [6]; Q is volume flow rate along the jet; and η^* is the extensional viscosity. The force and momentum terms affected by solvent evaporation rate are highlighted in equation (11).

The extensional viscous force (term 2. F_{vis} in equation (11)) is affected by change in the extensional viscosity (η^*) and the net evaporation rate ($\frac{dQ}{ds}$). [12]. The net evaporation rate is determined by the mass transfer/ evaporation rate terms, equation (9). The extensional viscosity (η^*) is related to the non-dimensional parameter Trouton ratio (Tr) to the shear viscosity (η_0), by $\eta^* = \eta_0 \times \widehat{Tr}$ [6], where η_0 is a measured shear viscosity and changes with polymer concentration. Since we have no way to measure Tr, we use a fitted Trouton ratio, $\widehat{Tr}$, by comparing modeling results and experimental observations.

The fitted Trouton ratio, $\widehat{Tr}$, is determined by comparing model results to the observations of the jet diameter change rate ($\frac{dd}{ds}$) at the end of straight jet region and final fiber diameter. A value $\widehat{Tr}\sim 10$ is found to work well for PVP/methanol and PVP/ethanol solutions, and a value of $\widehat{Tr}\sim 100$, is found to work well for PVP/1-butanol solutions. These fitted Trouton ratio values achieve good modeling results over a broad range of operating conditions, in terms of flow rate and RH (which significantly affects the evaporation rate and thus $\frac{\partial Q}{\partial s}$), which results in different extensional viscous force conditions [12].

In the bending region, the shear viscosity (η_0) increases as the polymer concentration increases due to solvent evaporation, but also changes due to the relatively smaller water mole concentration change due to water absorption. The measured solution shear viscosity is shown as a function of polymer concentration [12] and yields: $\eta_0 \sim c^{2.65}$ for PVP/methanol, $\eta_0 \sim c^{2.67}$ for PVP/ethanol, $\eta_0 \sim c^{3.58}$ for PVP/1-butanol.

3.3 Experimental verification

To verify the model, model and experimental results were compared for a variety of PVP/alcohol solutions conducted over a broad range of operating conditions and solution properties. In particular, flow rate varied by a factor of 2.3, voltage varied from the lower to upper bounds, RH varied by a factor of 2, solution shear viscosity varied by a factor of 6.3, conductivity varied by a factor of 6.6, solvent evaporation rate varied by a factor of 11.3, and water absorption rate varied by a factor of 17.9. This resulted in a large range of the final fiber diameter, which varied by a factor of 7.

Fig. 8 shows the comparison of molded results to experimental fiber diameters for the different RH and solvents, which shows that RH has a relatively larger impact than flow rate and voltage. The average absolute fiber diameter error is less than 8% for this a broad range of operating conditions and solution properties. This suggests that the developed model captures the dominant process physics in the bending region for non-aqueous hydrophilic PVP/alcohol solutions.

In order to understand the impact that the range of solution properties have on the experiments, the terms of the force balance (equation 11) and mass balance (equation 9) are used to evaluate the impacts expressed in terms of forces and jet length. Since ~ 90% jet diameter thinning occurs in the transition region and the lower bending region (fig. 10), the forces in terms of extensional viscous force, charge-to-charge force and net stretching force are characterized at the mid-point of the transition region and lower bending region for each PVP/alcohol solution case. To understand the relative impact, the forces are normalized by the electric force of PVP/methanol solutions, which has the largest stretching force in those PVP/alcohol solution cases. The jet length is normalized by the calculated jet length of PVP/1-butanol solution, which has smallest net evaporation rate and thus, has the longest jet length.

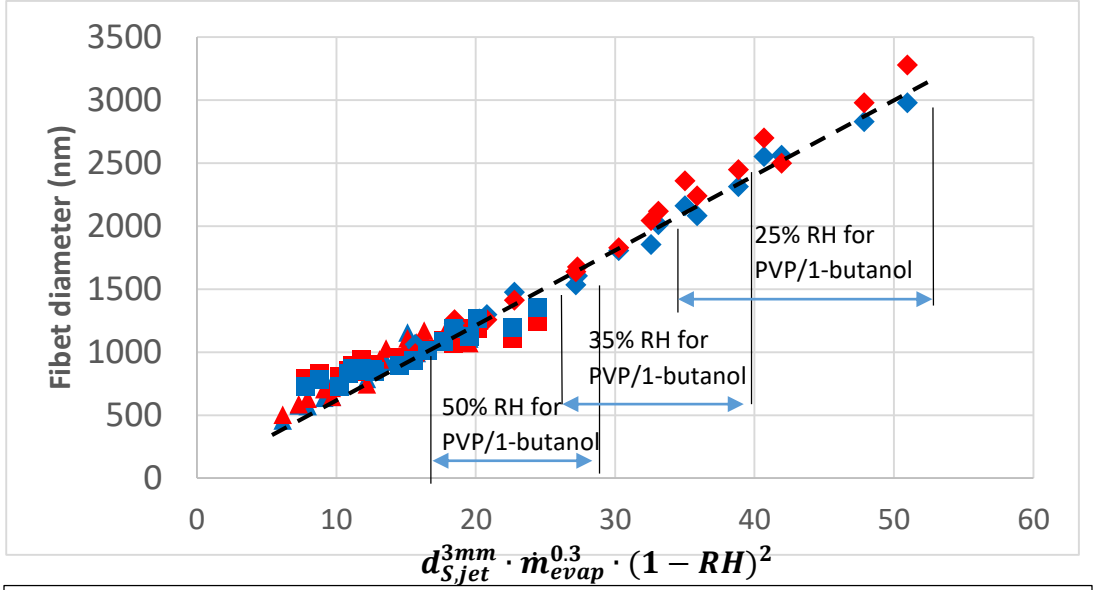

Fig. 8 Comparison experimental measurements (blue) and modeling predictions (red) of fiber diameters for PVP/methanol (▲), PVP/ethanol (■), and PVP/1-butanol (◆) solutions under different operating conditions (upper and lower voltage bounds for RH: 25% - 50%, Q: 0.03 – 0.07 ml/min). The absolute average fiber diameter error is less than 8%

Fig. 9 shows the normalized jet length, extensional viscous force, electric stretching force, and the net force for the 3 PVP/alcohol solution cases and it is interesting to compare these results to the range of property values (fig. 1). Since the bending region jet length is determined by net evaporation rate, PVP/1-butanol has a longer jet length (4.8 times) than PVP/ethanol due to its smaller net evaporation rate (7 times). Comparison of the solution properties to the forces indicates that solution properties are not sufficient to determine

forces. Although PVP/1-butanol has a much larger shear viscosity (7.9 times) than PVP/methanol, the extensional viscous force of PVP/1-butanol is 10.6 times larger than that of PVP/methanol, since the extensional viscous force is also affected by Trouton ratio and net evaporation rate (equation 11). In addition, although a larger conductivity leads to a larger current, the conductivity is not sufficient to determine electric force, which is determined in part by charge density and electric field (equation 11). PVP/1-butanol has a smaller (15 times) conductivity than PVP/methanol, which results in a smaller (4 times) electric force. For PVP/alcohol solutions, since PVP/1-butanol has the smallest electric force and the largest electric force, it has the smallest net stretching force.

It is also noticed that the extensional viscous forces of PVP/methanol and PVP/ethanol are much smaller (~ 10 times) than the electric forces for them due to their relatively large conductivity and small viscosity. Thus, for PVP/methanol and PVP/ethanol, the extensional viscous force is not important. However, the extensional viscous force and electric force for PVP/1-butanol are at the same order of magnitude.

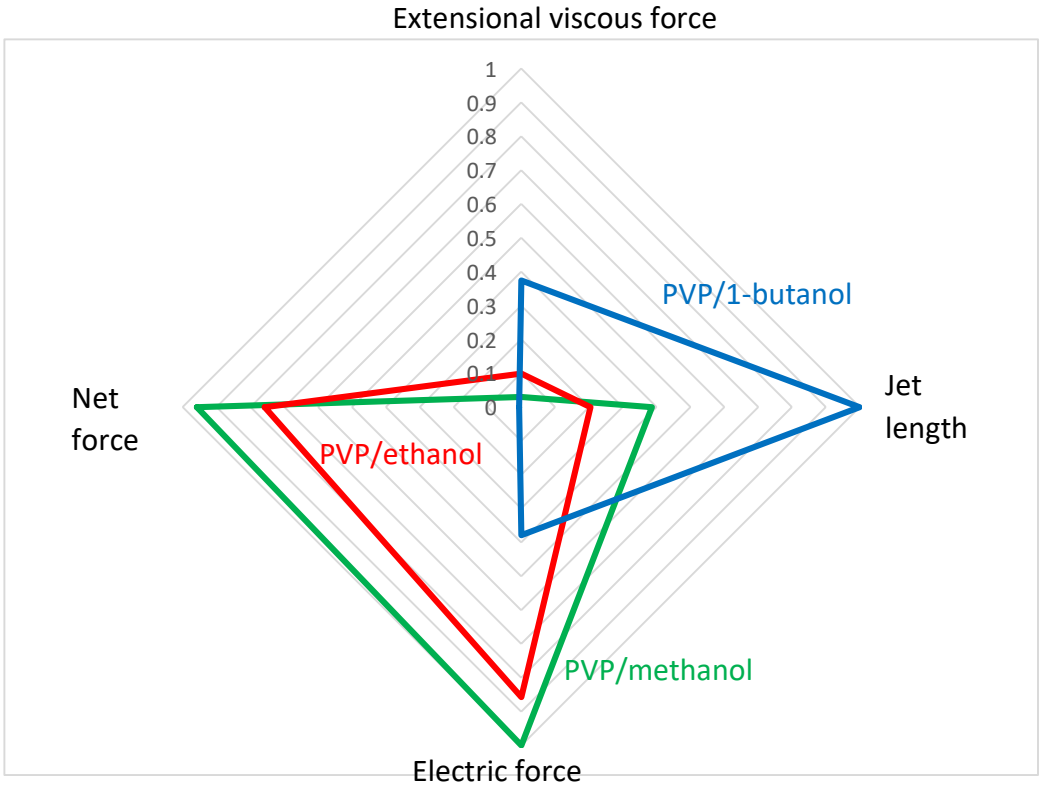

Fig. 9 Normalized extensional viscous force, electric force and net force, as well as jet length for PVP/methanol, PVP/ethanol and PVP/1-butanol solutions (0.05 ml/min and 35% RH)

4. Model analysis

This section analyzes the role of water absorption, RH, alcohol evaporation and jet stretching in determining the resulting fiber diameter using the modeling results of PVP/ethanol solutions. PVP/ethanol solutions have forces in-between those of PVP/methanol and PVP/1-butanol, but has the largest net evaporation rate and therefore the shortest jet length. The detailed modeling results for PVP/methanol and PVP/butanol are given in chapter 8 in [12]).

4.1 Contributions of mass transfer and stretching

The modeled jet diameter and net force for PVP/ethanol in the bending region is shown in fig. 10, illustrating the degree of stretching and evaporation. The jet diameter with solvent removed represents the contribution of jet stretching, and shows that ~28% of diameter change in the bending region is due to stretching. Although the contribution of stretching is smaller than that of net evaporation, the bending region jet stretching is important since the jet diameter only decreases to nano-scale at the late stage of bending region.

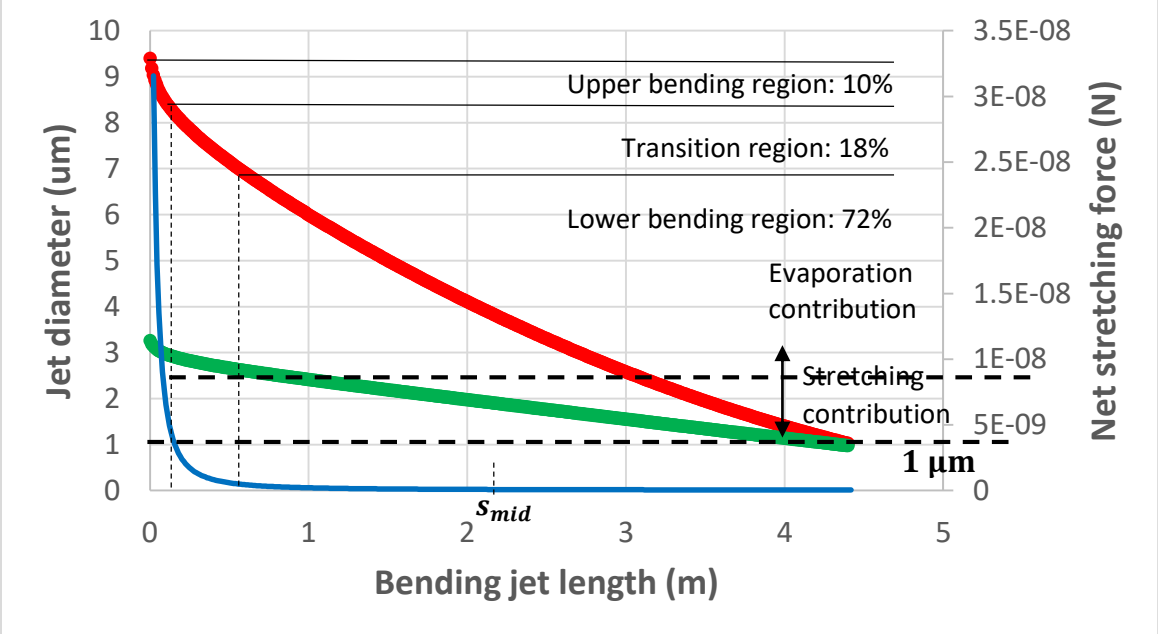

Fig. 10 Model prediction of jet diameter (red), jet diameter with solvent removed (green), and net stretching force (blue) in the bending region for PVP/ethanol solutions (35% RH, 0.05 ml/min and 12 kV).

Comparing the shape of the net stretching force and jet diameter curves (fig.10) reveals that although the net force is very small through most the length of the jet in the bending region, it has a significant impact in terms of jet stretching. The bending region can be separated into 3 regions: upper bending region with large net force decrease, transition region and lower bending region with a small net force. Although the length in the upper bending region is short (~0.1 m which is 2.3% of the bending jet length), the jet diameter decreases 10% due to the large net stretching force. However, 72% of the jet diameter decreases in the lower bending region due to its long jet length (~ 3.5 m which is 81% of the bending jet length), even though the net force is ~ 3 orders of magnitude smaller.

Comparing the jet shape and net stretching force (fig.10) with the net evaporation rate curve (fig. 11(a)) reveals that the jet thinning rate follows the evaporation rate. Fig. 10 shows that the jet diameter has a sharp but limited decrease in the upper bending region due to the large net stretching force. This observation is similar to the measured jet shape in the straight jet region (see appendix A in [12]). However, in the straight jet region, evaporation is negligible, the jet diameter decreases dramatically ~ 160 times due to the large net stretching force [11] over a short portion of the straight jet length, and then slowly decrease. In contrast, the jet diameter decreases at limited levels for much of the bending region. Fig. 11(a) shows that the net evaporation rate decreases slowly in the bending region since the evaporation rate only is weakly determined by jet shape, $\dot{m}_{net,n} \sim R_n^{1/3}$ (equation (9)). This results in a limited decrease in jet diameter in the transition and lower bending regions. In summary, the large change of net stretching force in the upper bending region has a relatively small effect on jet thinning rate relative to the effect of net evaporation rate.

4.2 Effect of RH on mass and force balances

To determine how RH affects the electrospinning process and final fiber diameter for PVP/alcohol solutions, the jet behavior for 3 different RH cases for PVP/ethanol solutions are analyzed. The experimental conditions and modeling results for those 3 cases are given in table. 3 which show the corresponding jet behavior for the bending region. As RH increases from 25% to 50%, the jet length increases ~20% and the fiber diameter decreases ~25%.

Table. 3 Experimental measurements and modeling results for PVP/ethanol solutions under 3 different RH levels

RH	Q (ml/min)	V (kV)	I (nA)	$d_{S,jet}^{3mm}$ (um)	$d_{S,jet}$ (final) (um)	Calculated L_{jet} (m)	Measured d_{fiber} (nm)	Calculated d_{fiber} (nm)
50%	0.05	11.6	90.7	30.9	9	4.96	869	893
35%	0.05	12	92.3	27.1	9.4	4.39	1010	1020
25%	0.05	12	97.2	24.8	9.8	3.99	1270	1190

The plot of net evaporation rate as a function of jet length as a function of RH (fig. 11(a)) shows that a higher RH leads to a decrease in net evaporation rate. A decrease of net evaporation rate results in a longer jet length and stretching time. Why does net evaporation rate decrease with higher RH? The mole fraction of ethanol on the jet surface decreases for greater RH since the mole fraction of absorbed water increases (fig. 11(b)). This results in the net evaporation rate decreasing for greater RH since the decrease in alcohol evaporation rate are greater than the amount of water absorption as shown in fig. 11(c).

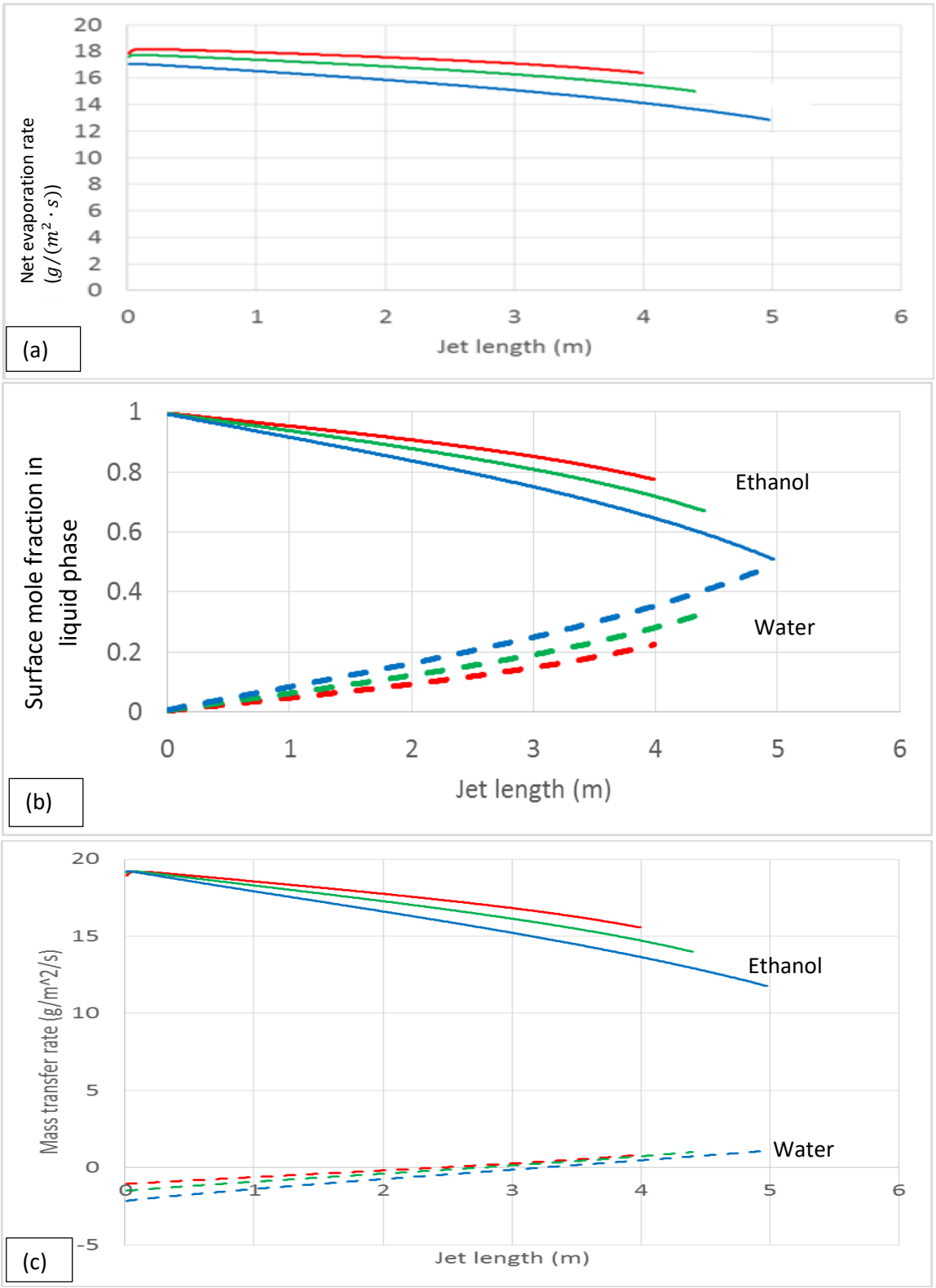

Fig. 11 (a) modeling net evaporation rates for PVP/ethanol solutions under different RH conditions; (b) modeling water and ethanol mole fractions on surface for different RH conditions; (c) modeling water absorption rate and ethanol evaporation rate for different RH conditions. (Red: 25% RH; green: 35% RH; blue: 50% RH, positive: evaporation, negative: absorption)

When does the absorbed water start to evaporate from the jet? When the water mole fraction on surface is larger than that in the air, the water starts to evaporate from the jet which occurs at ~ 3m. Fig. 11 (c) also shows that the water absorption rate is ~ 10 times smaller than the solvent evaporation rate on the jet surface, which occurs since water absorption is limited by diffusion ($Bi_m \gg 1$) and solvent evaporation rate is determined by the solvent mole concentration on surface. Thus, the major reason for the decrease of net evaporation rate with increasing RH is the decrease of ethanol evaporation rate due to larger amount of water occupying the surface states. Although the amount of absorbed water is small relative to the solvent, RH significantly affects the net evaporation rate since RH significantly changes the surface state distribution which ultimately determines the solvent evaporation rate (equation (8)).

The net stretching force is also found to increase as RH increases, as shown in fig. 12. At 3m (which is ~70% of bending jet length), the calculated net stretching force increases a modest ~7% as RH increases from 25% to 50%. The increase of net stretching force with increasing RH is a result of the decrease in both electric stretching and extensional viscous retarding forces. Since the extensional viscous retarding force decreases by ~40%, which is larger than the decrease (~4.7%) in electric stretching force (fig. 13), the net stretching force increases as RH increases (fig. 12).

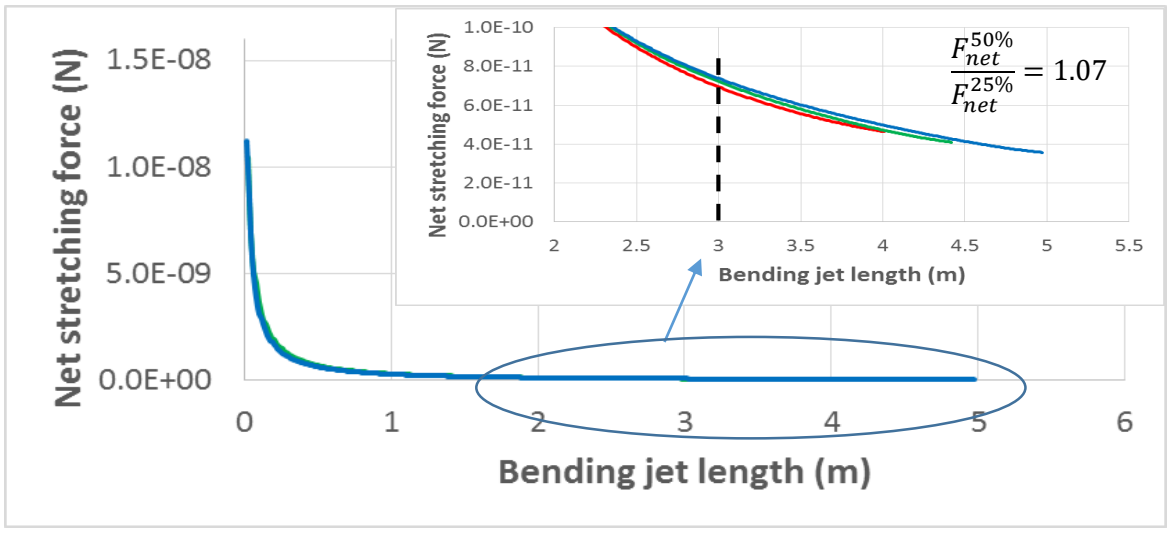

Fig. 12 modeled net stretching forces for PVP/ethanol solutions under 25% RH (red), 35% RH (green) and 50% RH (blue). As RH increases from 25% to 50%, the calculated net stretching force increases ~ 7% at 3 m in the bending region (upper bounds of 0.05 ml/min).

Overall, both the total jet length and net stretching force determine the final fiber diameter. Understanding the magnitude of the effect that RH has on the net stretching force and jet length is important for understanding the overall impact of RH. For PVP/ethanol solutions, as RH increases from 25% to 50%, although the extensional viscous force decreases ~40%, the net stretching force only increases a modest ~7% since the electric force is much larger (~10 times) than the extensional viscous force due to the relatively small viscosity and large conductivity (fig. 1). However, this increase in the net stretching force cannot explain the ~25% decrease in fiber diameter (fig. 10) itself. The major factor is the ~20% increase in jet length (which increases the stretching time).

While PVP/methanol has similar results (see chapter 8 in [12]), PVP/1-butanol behaves significantly different since the electric force has a similar magnitude on the extensional viscous force due to the relatively large viscosity and relatively small conductivity (fig. 1). For PVP/1-butanol, as RH increases from 25% to 50%, the net stretching force increases 45% due to the 31% decrease in extensional viscous force and 8% decrease in the electric force. The overall 60% decrease in fiber diameter results from the 45% increase in net stretching force and 20% increase in jet length.

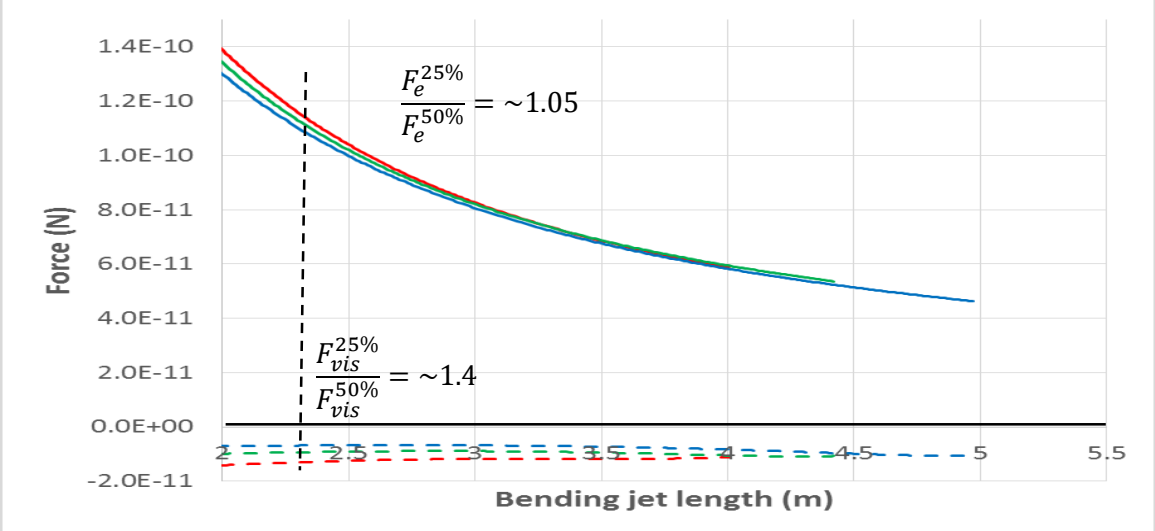

Fig. 13 Plot of viscous retarding and electric stretching forces as a function of RH (red: 25% RH, green: 35% RH, blue: 50% RH). Net stretching force increases since reduction of extensional viscous force with increasing RH is greater than that of electric force.

The model analysis provides insight as to what drives the change in force as RH changes. Both the electric field force and charge-to-charge force vary with the surface charge density (σ_s, see equation (10)). As RH increases, the net evaporation rate decreases, which results in a decrease in surface charge density (fig. 14), and thus the electric force, since the surface charge density is a function of jet flow rate (equation (11)). The extensional viscous force (equation (10)) is determined by shear stress ($\tau = \frac{6\eta^*}{R}\frac{dv_s}{ds}\frac{dR}{ds} + 3\eta^*\frac{d^2v_s}{ds^2}$) [6]. Thus, as RH increases, the net evaporation rate decreases, which results in a smaller $\frac{dv_s}{ds}$ and $\frac{d^2v_s}{ds^2}$, and thus shear stress (fig. 15) and extensional viscous force decrease.

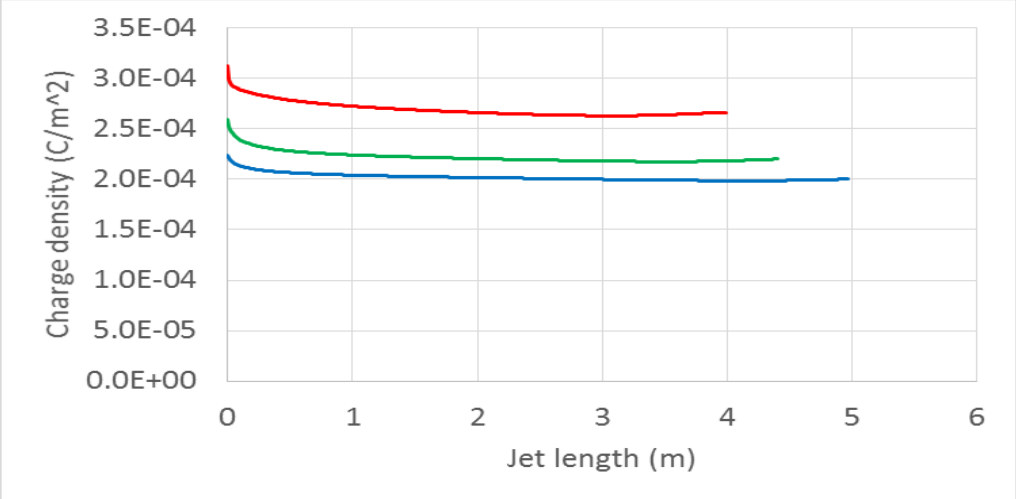

Fig. 14 Plot of modeling surface charge density for PVP/ethanol solutions along the jet for 25% RH (red), 35% RH (green) and 50% RH (blue).

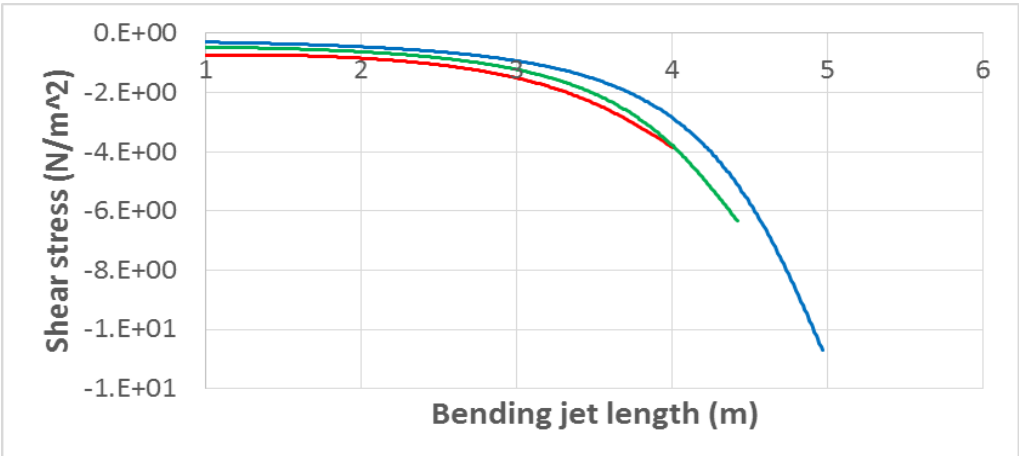

Fig. 15 Plot of modeling shear stress for PVP/ethanol solutions along the jet for 25% RH (red), 35% RH (green) and 50% RH (blue).

5. Summary

In this paper, a combined experimental and modeling analysis of the bending region for 3 different non-aqueous hydrophilic PVP/alcohol solutions is presented. Experimental observations reveal that both jet stretching and evaporation in the bending region is significant in determining the final fiber diameter. To obtain insight into the process physics, a model is developed that captures the coupled mass and force balances, and predicts the final fiber diameter to within 8% of experimental results over a broad range of operating conditions and solution properties. The mass balance includes the evaporation/ absorption of alcohol and water on surface, the radial diffusion of alcohol and water in jet, and the axial advection of alcohol and water in jet. Water diffusion in the jet is found to limit the absorption rate, and the species absorption and diffusion model is experimentally verified. The force balance is based on the dominant factors including extensional viscous force and the electric stretching forces (electric field and charge-to-charge forces).

Model analysis reveals that the net evaporation rate (sum of solvent evaporation rate and water absorption rate on surface) has two significant impacts. First, the net evaporation rate affects the jet length and the stretching time, wherein the longer the jet, the smaller the fiber diameter. Secondly, the net evaporation rate also affects the net stretching force, since the mass flow affects the charge density and viscous terms. The effect of net evaporation rate on extensional viscous retarding force is greater than the impact on the electric stretching force. For PVP/methanol and PVP/ethanol solutions, since the extensional viscous force is much smaller than the electric force, the effect of RH on net stretching force is relatively small. However, for PVP/1-butanol solutions, the effect of RH on net stretching force is significant. The larger RH results in a larger net stretching force and a smaller fiber diameter.

Analysis of the impact of RH reveals that although the amount of absorbed water is not large, it has a profound impact on the solvent evaporation rate and thus final fiber diameter. As the ambient RH increases, the water mole concentration on the surface increases, resulting in a decrease in alcohol mole concentration, which leads to a lower solvent evaporation rate and a higher water absorption rate. The decrease of net evaporation rate results in a longer jet and larger net stretching force. Thus, the final fiber diameters of non-aqueous hydrophilic PVP/alcohol solutions decrease as RH increases.

Using the model, the impact of different solution properties is determined in terms of the relation between forces and evaporation rate to the resulting fiber diameter.

Acknowledgements

We appreciate the funding support from the Army (W911QY-11-1-0014), and the contributions of Jinjiang Liu in conducting experiments. We also acknowledge the contribution of that Keith Forward made discussion of the mass transfer model development.

Reference

[1] Hohman, M.M., Shin, M., Rutledge, G. and Brenner, M.P., 2001. Electrospinning and electrically forced jets. I. Stability theory. Physics of Fluids (1994-present), 13(8), pp.2201-2220.

[2] Hohman, M.M., Shin, M., Rutledge, G. and Brenner, M.P., 2001. Electrospinning and electrically forced jets. II. Applications. Physics of Fluids (1994-present), 13(8), pp.2221-2236.

[3] Feng, J.J., 2002. The stretching of an electrified non-Newtonian jet: A model for electrospinning. Physics of Fluids (1994-present), 14(11), pp.39e-3926.

[4] Rutledge, G.C. and Fridrikh, S.V., 2007. Formation of fibers by electrospinning. Advanced Drug Delivery Reviews, 59(14), pp.1384-1391.

[5] De Vrieze, S., Van Camp, T., Nelvig, A., Hagström, B., Westbroek, P. and De Clerck, K., 2009. The effect of temperature and humidity on electrospinning. Journal of materials science, 44(5), pp.1357-1362.

[6] Cai, Y. and Gevelber, M., Analysis of bending region physics in determining electrospun fiber diameter: effect of relative humidity on evaporation and force balance. Journal of Materials Science, pp.1-23.

[7] Wang C.W, Hsu C.H, and Lin J.H. Scaling laws in electrospinning of polystyrene solutions. Macromolecules, 39:7662{7672, 2006.

[8] Yarin, A.L., Koombhongse, S. and Reneker, D.H., 2001. Bending instability in electrospinning of nanofibers. Journal of Applied Physics, 89(5), pp.3018-3026.

[9] Forward, K.M., Flores, A. and Rutledge, G.C., 2013. Production of core/shell fibers by electrospinning from a free surface. Chemical Engineering Science,104, pp.250-259.

[10] Yan X. "Electrospinning of nanofibers: analysis of diameter distribution and process dynamics for control. " Thesis (Ph. D.) Boston University, 2011.

[11] Cai Y. "Electrospinning process analysis: the relation of process parameters to fiber diameter and process dynamics for closed-loop control design. " Thesis (Master) Boston University, 2013.

[12] Cai, Y., 2017. Modeling and experimental analysis of electrospinning bending region physics in determining fiber diameter for hydrophilic polymer solvent systems (Doctoral dissertation, Boston University).

[13] Smallwood, I., 2012. Handbook of organic solvent properties. Butterworth-Heinemann.
[14] Cai, Y. and Gevelber, M., 2013. The effect of relative humidity and evaporation rate on electrospinning: fiber diameter and measurement for control implications. Journal of Materials Science, 48(22), pp.7812-7826.
[15] Fredenslund, A., 2012. Vapor-liquid equilibria using UNIFAC: a group-contribution method. Elsevier.